Particle Monte Carlo and lattice-Boltzmann methods for simulations of gas–particle flows

Udo Lantermann, Dieter Hänel *

Institute of Combustion and Gasdynamics, University of Duisburg-Essen, D-47057 Duisburg, Germany

Abstract

A numerical solution concept is presented for simulating the transport and deposition to surfaces of discrete, small (nano-)particles. The motion of single particles is calculated from the Langevin equation by Lagrangian integration under consideration of different forces such as drag force, van der Waals forces, electrical Coulomb forces and not negligible for small particles, under stochastic diffusion (Brownian diffusion). This so-called particle Monte Carlo method enables the computation of macroscopic filter properties as well the detailed resolution of the structure of the deposited particles. The flow force and the external forces depend on solutions of continuum equations, as the Navier–Stokes equations for viscous, incompressible flows or a Laplace equation of the electrical potential. Solutions of the flow and potential fields are computed here using lattice-Boltzmann methods. Essential advantage of these methods are the easy and efficient treatment of three-dimensional complex geometries, given by filter geometries or particle covered surfaces. A number of numerical improvements, as grid refinement or boundary fitting, were developed for lattice-Boltzmann methods in previous studies and applied to the present problem. The interaction between the deposited particle layer and the fluid field or the external forces is included by recomputing of these fields with changed boundaries. A number of simulation results show the influence of different effects on the particle motion and deposition.
© 2006 Elsevier Ltd. All rights reserved.

1. Introduction

Transport and deposition of nano-particles in a gas phase play an important role in experimental and industrial processes for manufacturing of surface structures or for extraction and analysis of the particle phase.

The mathematical modeling of the complex physical problem is based on the assumption of small particle concentrations which results in a decoupling of the phases. The gas phase (carrying phase) and the external forces are computed independently from the solid phase (carried phase). The transport of the latter one is determined then using the known fields of flow and forces. Interaction between the phases is considered near surfaces where particles are

depositing. The deposited particles change the surface geometry and thus the boundary conditions for fluid flow and potential forces. This influence is taken into account by recomputing of the fluid and potential fields after a fixed amount of deposited particles.

The particle transport is described by the Langevin equation. The numerical integration of this equation was performed by Ermak and Buckholz [10] with a Monte Carlo simulation technique under consideration of Brownian diffusion and an arbitrary external force. This method has been used in all of the following papers. It was applied to particle deposition onto spherical collectors under influence of different forces by Gupta and Peters [20]. They used analytical solutions for the electric field and the fluid field. The deposition of submicron particles on collectors in two-dimensional flow was considered by Chang and Whang [5]. The fluid field is determined by the Kuwabara flow model, van der Waals force was included in the external force.

* Corresponding author. Tel.: +49 203 379 3428; fax: +49 203 379 3087.
  E-mail addresses: haenel@vug.uni-duisburg.de, haenel@ivg.uni-duisburg.de (D. Hänel).

Zarutskaya and Shapiro [42] performed simulations of submicron particle deposition on filters under the influence of magnetic forces. The 2D fluid field and magnetic field are calculated as steady-state solutions of the Navier–Stokes equations and the Poisson equation, respectively. The model was validated for dilute particle concentration and large ratios of fiber and particle diameters.

The influence of Reynolds number, fiber aspect ratio, filter packing density and particulate size on the particle deposition on two-dimensional rectangular fibers in a staggered arrangement was investigated by Chen et al. [7].

Wu et al. [40] simulated particle deposition on a charged fiber in the two-dimensional case and Oh et al. [36] considered 2D and 3D models. They took into account earlier deposited particles for the particle deposition so that fractal-like structures appeared at the surfaces. This dendrite-like formations played a significant role in the collection process. But the boundary conditions for fluid field and electric field did not change due to the deposited particles, so there were no influence between the deposited particles and these fields.

Przekop et al. [37] developed a lattice-Boltzmann approach for the simulation of 2D particle motion through a fibrous filter. Their method includes the influence of deposited particles at the surface on the fluid field. Beside the friction force they considered diffusional replacement of the moving particles and the breaking-off force for particle resuspension. However, their particle motion model is lattice-based, i.e. a particle is represented by one node with a radius of the half lattice spacing $r_p = \delta x/2$. Therefore it results in a large amount of grid nodes especially in 3D cases or if the ratio between fiber diameter and particle diameter is large.

Another method for calculating particle transport and deposition, based on a lattice-Boltzmann model, was proposed by Masselot and Chopard [33] for snow in air. They integrated the particle model in the LBGK method taking into account transport, deposition and erosion. Changing boundary conditions due to these effects were included in their model. Dupuis and Chopard [8] extended the model for the simulation of interactions of sediment and water.

The flow of particle laden fluids through porous media is studied in [17]. The fluid phase is calculated by a lattice-Boltzmann method whereas the particle phase is determined by the method of moments. The latter one describes the time evolution of particle distributions which allows the consideration of particle aggregation during flight.

The paper is organized in the following way: The section two describes the integration of the Lagrangian equation of motion using a semi-analytical solution and numerical Euler forward integration. The same chapter presents details of the formulation of the random diffusion and the forces, as e.g. van der Waals forces near surfaces or electrical forces. The deposition model is based on van der Waals forces near surfaces or deposits and takes into account changes of boundary conditions due to particles deposited before. The flow field and potential fields of forces are computed using lattice-Boltzmann methods, described in section three. These methods include grid refinement for local high resolution and boundary fitting for accurate fitting of arbitrary boundary shapes. The combined method was validated by means of experimental and theoretical results for three-dimensional flow through filters. Further results are shown for the deposition of electrically charged particles.

2. Particle transport in the gas phase

2.1. Particle Monte Carlo method

An integration method for computing the particle motion in a gas environment has been developed with the aim to study in detail the transport and deposition of particles, as well the formation of particle structures on surfaces. The motion of particles is influenced by different forces such as fluid drag, random Brownian diffusion or electrical forces. The requirements to the particle method are satisfied by Lagrangian tracking of individual, solid particles and computing the trajectories of each particle. The particle paths are determined by Lagrangian integration of the Langevin equation, similar as performed in [20].

Large numbers of particle trajectories have to be computed partially for statistical reasons, so a few assumptions are introduced to reduce the numerical effort. The most important assumption is the assumption of dilute particle concentration so that interactions between particles in flight can be neglected. However influence of deposited particles (due to changed boundary conditions) on particles approaching the surface is allowed. Further the particles are assumed to be of spherical shape and in translatoric motion only.

The particle motion is described by the Lagrangian equations of motion for a particle of mass m_p:

$$m_p \frac{d\mathbf{v}(t)}{dt} = \mathbf{F}_d(t, \mathbf{x}(t)) + \mathbf{F}_{ext}(t, \mathbf{x}(t)) + m_p \mathbf{A}(t) \qquad (1)$$

where the particle path $\mathbf{x}(t)$ is given by

$$\frac{d\mathbf{x}(t)}{dt} = \mathbf{v}(t) \qquad (2)$$

The drag force $\mathbf{F}_d(t, \mathbf{x}(t))$ is proportional to the difference of fluid velocity $\mathbf{u}$ and particle velocity $\mathbf{v}$

$$\mathbf{F}_d = m_p \beta(\mathbf{u} - \mathbf{v}) \quad \text{with} \quad \beta = \frac{6\pi\mu r_p}{Cm_p}$$

The friction coefficient β, related to the particle mass, is determined from the Stokes law with the dynamic viscosity of the gas μ, the particle radius r_p and the particle mass m_p. The slip correction factor C has to be taken into account for particles whose diameters are of the same order or smaller than the mean free path λ of the gas molecules. It is calculated depending on the Knudsen number $Kn = \lambda/r_p$ by

$$C = 1 + Kn\left[A_1 + A_2 \exp\left(-\frac{2A_3}{Kn}\right)\right]$$

with constants A_1, A_2 and A_3, estimated in [16]. External forces $\mathbf{F}_{\text{ext}}$, as van der Waals forces or electric forces are described in the next section. $\mathbf{A}(t)$ is a stochastic acceleration term depending on time only and represents the Brownian motion.

Eqs. (1) and (2) are rearranged in a coupled system of ordinary differential equations, where $\mathbf{I}$ is a identity matrix. The first equation is called Langevin equation. Eqs. (1) and (2) have to be integrated in time to determine velocity $\mathbf{v}(t)$ and position $\mathbf{x}(t)$ of each particle.

$$\begin{pmatrix} \frac{d\mathbf{v}(t)}{dt} \\ \frac{d\mathbf{x}(t)}{dt} \end{pmatrix} = \underbrace{\begin{pmatrix} -\beta\mathbf{I} & 0 \\ \mathbf{I} & 0 \end{pmatrix}}_{\mathbf{T}_1}\begin{pmatrix} \mathbf{v}(t) \\ \mathbf{x}(t) \end{pmatrix} + \underbrace{\begin{pmatrix} \beta\mathbf{u}(t) + \mathbf{F}_{\text{ext}}(t)/m_{\text{p}} \\ 0 \end{pmatrix}}_{\mathbf{T}_2} + \underbrace{\begin{pmatrix} \mathbf{A}(t) \\ 0 \end{pmatrix}}_{\mathbf{T}_3}$$

(3)

The fluid velocity and the forces are assumed to be constant during the integration over a time step $\Delta t = t - t_0$ if the time step is sufficiently small in the order of β^{-1}. The system (3), neglecting the stochastic term $\propto\mathbf{A}(t)$, can be solved analytically similar as in [29] and yields:

$$\begin{pmatrix} \mathbf{v}(t) \\ \mathbf{x}(t) \end{pmatrix} = \mathbf{\Phi}(t)\left[\begin{pmatrix} \mathbf{v}(t_0) \\ \mathbf{x}(t_0) \end{pmatrix} + \int_{t_0}^{t} \mathbf{\Phi}^{-1}(\tau)\mathbf{T}_2(\tau)\,d\tau\right]$$

where the matrix $\mathbf{\Phi}(t)$ and its inverse is

$$\mathbf{\Phi}(t) = \begin{pmatrix} e^{-\beta(t-t_0)}\mathbf{I} & 0 \\ \frac{1}{\beta}(1 - e^{-\beta(t-t_0)})\mathbf{I} & \mathbf{I} \end{pmatrix},$$

$$\mathbf{\Phi}^{-1}(t) = \begin{pmatrix} e^{\beta(t-t_0)}\mathbf{I} & 0 \\ \frac{1}{\beta}(1 - e^{\beta(t-t_0)})\mathbf{I} & \mathbf{I} \end{pmatrix}.$$

The solution with the definition of term $\mathbf{T}_2$ reads then

$$\begin{pmatrix} \mathbf{v}(t) \\ \mathbf{x}(t) \end{pmatrix} = \mathbf{B}(t)\begin{pmatrix} \mathbf{v}(t_0) \\ \mathbf{u}(t_0) + \frac{1}{m_{\text{p}}\beta}\mathbf{F}_{\text{ext}}(t_0) \end{pmatrix} + \begin{pmatrix} 0 \\ \mathbf{x}(t_0) \end{pmatrix}$$

(4)

with

$$\mathbf{B}(t) = \begin{pmatrix} e^{-\beta(t-t_0)}\mathbf{I} & (1 - e^{-\beta(t-t_0)})\mathbf{I} \\ \frac{1}{\beta}(1 - e^{-\beta(t-t_0)})\mathbf{I} & [(t - t_0) - \frac{1}{\beta}(1 - e^{-\beta(t-t_0)})]\mathbf{I} \end{pmatrix}$$

The stochastic term $\mathbf{T}_3$ can be determined in analogous manner due to Itô's rule in [29], which results in

$$\int_{t_0}^{t} \mathbf{T}_3(\tau)\,d\tau = \begin{pmatrix} \int_{t_0}^{t} e^{-\beta(t-\tau)}\mathbf{A}(\tau)\,d\tau \\ \frac{1}{\beta}\int_{t_0}^{t}(1 - e^{-\beta(t-\tau)})\mathbf{A}(\tau)\,d\tau \end{pmatrix}.$$

(5)

The integrals of Eq. (5) cannot be solved directly, since the random function $\mathbf{A}(t)$ has a mean equal to 0 and is not continuous. The statistical properties of the integrals are discussed in detail in [4]. Application to the particular case of Eq. (5) as in [42], yields a formulation of the random movement, validated and used in the succeeding computations:

$$\int_{t_0}^{t} \mathbf{T}_3(\tau)\,d\tau = \begin{pmatrix} \mathbf{z}_1\sigma_v \\ \mathbf{z}_1\frac{\sigma_{vx}}{\sigma_v} + \mathbf{z}_2\sqrt{\sigma_x^2 - \frac{\sigma_{vx}^2}{\sigma_v^2}} \end{pmatrix}$$

(6)

where

$$\sigma_v = \sqrt{\frac{kT}{m_{\text{p}}}(1 - e^{-2\beta(t-t_0)})}$$

$$\sigma_x = \frac{1}{\beta}\sqrt{\frac{kT}{m_{\text{p}}}(2\beta(t - t_0) - 3 + 4e^{-\beta(t-t_0)} - e^{-2\beta(t-t_0)})}$$

$$\sigma_{vx} = \frac{kT}{m_{\text{p}}\beta}(1 - e^{-2\beta(t-t_0)})^2$$

with the Boltzmann constant k and the temperature T. The components of $\mathbf{z}_1$ and $\mathbf{z}_2$ are normally distributed random numbers with mean equal 0 and variance equal 1.

The complete solution of Eq. (3) results from the superposition of Eqs. (4) and (6). The final solution with index n for temporal discretization level is given by

$$\begin{pmatrix} \mathbf{v}^{n+1} \\ \mathbf{x}^{n+1} \end{pmatrix} = \mathbf{B}^n\begin{pmatrix} \mathbf{v}^n \\ \mathbf{u}^n + \frac{1}{m_{\text{p}}\beta}\mathbf{F}_{\text{ext}}^n \end{pmatrix} + \begin{pmatrix} 0 \\ \mathbf{x}^n \end{pmatrix}$$

$$+ \begin{pmatrix} \mathbf{z}_1\sigma_v \\ \mathbf{z}_1\frac{\sigma_{vx}}{\sigma_v} + \mathbf{z}_2\sqrt{\sigma_x^2 - \frac{\sigma_{vx}^2}{\sigma_v^2}} \end{pmatrix}$$

where

$$\mathbf{B}^n = \begin{pmatrix} e^{-\beta\Delta t}\mathbf{I} & (1 - e^{-\beta\Delta t})\mathbf{I} \\ \frac{1}{\beta}(1 - e^{-\beta\Delta t})\mathbf{I} & [\Delta t - \frac{1}{\beta}(1 - e^{-\beta\Delta t})]\mathbf{I} \end{pmatrix}$$

The expressions σ_v, σ_x, σ_{vx} depend only on the discrete time step Δt.

2.2. Interaction and external forces

Different forces acting on the discrete particles are considered. Detailed modeling of these forces is taken over from the literature, as e.g. from [3,16,9,28].

2.2.1. Gravitational force and buoyancy force
The gravitational force and the buoyancy force due to the displaced fluid volume are combined in one force

$$\mathbf{F}_{\text{g}} = -(m_{\text{p}} - m_{\text{g}})\mathbf{g}$$

The displaced fluid mass of spherical particles of volume $V_{\text{p}} = \frac{4}{3}\pi r_{\text{p}}^3$ is $m_{\text{g}} = \rho_{\text{g}}V_{\text{p}}$ with the gas density ρ_{g}, the particle radius r_{p} and the gravitational constant $\mathbf{g}$. This force is proportional to r_{p}^3 and is negligible in general for very small particles as considered here.

2.2.2. Electrical forces
Electrical forces become relevant for charged particles moving in an electric field. Two forces, the Coulomb and the image force, are included.

The Coulomb force

$$\mathbf{F}_{\text{cou}} = -qe\nabla\phi$$

(7)

causes the migration of a particle in an external electric field. Here e is the electronic charge, q is the number of electronic charges accumulated by the particle and ϕ is the electric potential which can be determined by a Laplace equation (15).

In the vicinity of a surface with the dielectric constant ϵ_2 a charged particle moving in a fluid of dielectric constant ϵ_3 induces an image charge. This charge is located in a distance d on the other side of the boundary, where d is the distance between the center of the particle and the surface. The force of this interaction is given by

$$\mathbf{F}_{\text{im\_ps}} = \frac{-(qe)^2}{(4\pi\epsilon_0\epsilon_3)(2d)^2}\left(\frac{\epsilon_2 - \epsilon_3}{\epsilon_2 + \epsilon_3}\right)\mathbf{n}$$

where ϵ_0 is the static dielectric constant and $\mathbf{n}$ is the normal vector directed from the particle center to the surface.

2.2.3. Van der Waals forces

Van der Waals forces act over distances short compared to the particle diameter. These forces cannot be neglected for very small particles and, if the distance between the particles or rigid surface is sufficiently small. Therefore it plays essentially a role in the deposition process, when a particle approaches the surface or another particle, deposited earlier.

Two different numerical approaches for modeling van der Waals forces were tested.

The first, simpler approach assumes an effective collision cross-section to model the effect of van der Waals forces. The particle radius or the wall surface is increased then by a distance d of order of magnitude of particle radius. Deposition is assumed if a particle contacts a rigid wall or a previously deposited particle in this distance. This model is computationally easier but suffers on the realistic determination of the effective cross-section. The sketch in Fig. 1 shows the principle when using an additional collision cross-section. The additional collision cross-section can be neglected for larger particles, then a "touch and stop" model is used for modeling deposition, as described in [11].

The second approach substitutes van der Waals forces by a continuous force model described in the following.

For particle–surface interactions the van der Waals force is described by

$$\mathbf{F}_{\text{vdw\_ps}} = \frac{2A}{3}\frac{r_{\text{p}}^3}{d^2(2r_{\text{p}} - d)^2}\mathbf{n} \tag{8}$$

and for particle–particle interaction by

$$\mathbf{F}_{\text{vdw\_pp}} = \frac{32A}{3}\frac{r_{\text{p}}^6}{d^3(4r_{\text{p}}^2 - d^2)^2}\mathbf{n}, \tag{9}$$

with the Hamaker constant A, the particle diameter r_{p}, the minimal distance d between the surface of the moving particle and the one of the macroscopic body or of the deposited particle. In general the distance d approaches to zero if the particle is deposited. The vector $\mathbf{n}$ is the normal unit vector directed from the moving particle to the surface of the deposited particle.

Eqs. (8) and (9) are called the un-retarded van der Waals forces and tend to overestimate these forces. [39] introduces a retardation factor $0 < \alpha_{sp} \leqslant 1$ which depends on the separating distance d between the particle and the wall and between two particles, respectively. This factor is multiplied to Eqs. (8) and (9).

2.2.4. Back-influence of particle deposits

The back-influence of particle deposits on fluid flow and potential forces is taken into account by the corresponding change of boundary conditions. Particles deposited on the rigid surface or on previously deposited particles form irregular and complex structures, depending on the particle size, the fluid flow and the external forces, see e.g. results in Figs. 9 or 10. On the other hand, the changed surface structures alter the boundary conditions and influence interactively the next particle deposition.

These interactions are taken into account by recomputing the flow and electrical fields with the new boundary conditions each time after a certain number of particles has been deposited during the computations. The relatively easy, numerical realization of such complex boundary geometries, as well for fluid flow as for potential fields, is one of the advantages of the lattice-Boltzmann methods, described in the next section.
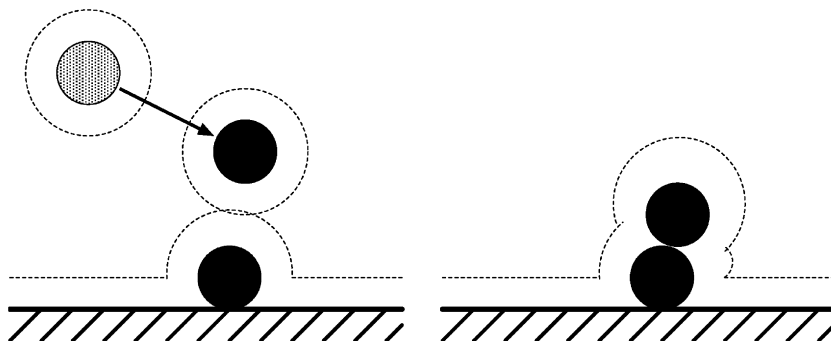

Fig. 1. Modeling of van der Waals forces for an incoming particle (left) and for a deposited particle at the wall (right).

The back-influence of particle deposits is of different importance. If the particle diameter is relatively large for a given filter geometry, then the displacement effects of deposited particles, e.g. in form of increasing pressure drop as shown in [11,14] becomes large and has to be taken into account while for small (nano-)particles it is negligible. However this back-influence plays a role for charged particles even for small particles.

3. Lattice-Boltzmann method

Lattice-Boltzmann methods are used in the present paper for computing the viscous flow of an incompressible fluid around three-dimensional geometries and in a variant for solving the potential equations of electrical or magnetic fields. These methods are chosen because of their high efficiency and their flexibility with respect to complex geometries. The lattice-Boltzmann approaches are described in following subsections.

The lattice-Boltzmann (LB) method is a discrete solution method of the Boltzmann equation based on a simplified phase space and were published first at the end of the Eighties, using a discrete form of the collision operator of the Boltzmann equation by Mcnamara and Zanetti [34] and Higuera et al. [25]. Efficiency and simplicity of the LB algorithm could essentially increased with the introduction of the modified collision operator by Bhatnagar Gross and Krook in [2]. Corresponding discrete LB methods, called lattice-BGK (LBGK) methods were published at the beginning of the Nineties by Qian et al. [38] and Chen et al. [6]. The corresponding connection between the discrete lattice-Boltzmann method and the Boltzmann equation is discussed for example in [1,24]. A variant of the LB methods, based on a moment formulation and on multiple relaxation times (MRT–LBE) was developed in the past years and published e.g. in [26,32,27]. The LBE with MRT collision model has better numerical stability and is thus more efficient than its LBGK counterpart, even though the computational cost of the MRT–LBE is about 10% higher than its LBE counterpart. A more recent review on LB methods is given e.g. in [41].

The classical LBGK method, used here, offers second order accuracy in space, high degree of parallelization and low computational costs in particular at moderate Reynolds numbers. The method is based on a discrete phase space in form of Cartesian-like lattices, which represent the spatial and molecular velocity space, as well. The method acts like a Cartesian grid solver and requires therefore additional algorithmic developments to deal with anisotropic flow fields over complex geometries. Typical such requirements are local grid refinement and boundary formulations for curvilinear boundary contours. Since LB methods operate on the molecular phase space, special developments of the LBGK method are required for it, compared to usual finite-volume or finite-element methods. Boundary formulations for LB methods were studied by several authors in [18,11,12,35,19] and others. The present

work uses the boundary fitting concept published in [13] with the extensions of [35]. Local grid refinement, adopted here, is based on the approach published in [13]. It can be optimized with respect to computational effort by an acceleration strategy presented in [15].

3.1. LBGK method for viscous, incompressible fluid flows

The viscous, incompressible fluid flow is assumed to be stationary or quasi-stationary. The Reynolds number Re is small of order $O(1)$ due to relatively small velocities and small dimensions, thus the flow remains laminar. The fluid flow is macroscopically described by the conservation equations for mass and momentum, called Navier–Stokes equations. It is well known from the kinetic theory of gases that the Navier–Stokes equations are solutions of the Boltzmann equation for sufficient small Knudsen numbers, [21]. In consequence, the Navier–Stokes equations are sufficiently well represented by the LBGK method as an approximation of the Boltzmann equation at small Knudsen numbers, [1]. The numerical LBGK approach is presented briefly in the following.

The phase space is approximated by an uniform, quasi-Cartesian grid with the lattice spacing δx. A discrete velocity distribution function f_{pi} is transported from a node along each link i to neighboring nodes with molecular velocities $\mathbf{c}_{pi}$ during a time step δt, see Figs. 2 and 3. Arriving the next node, the distribution function is changed by a collision model, given by the BGK collision operator. The index $p = \mathbf{c}_{pi}^2/c_0^2$ is the square modulus of the molecular velocity, where c_0 is the constant Cartesian component of the molecular velocity. It is $p = 0, 1, 2$ in 2D with 9 velocities and $p = 0, 1, 3$ in 3D with 15 velocities corresponding to Figs. 2 or 3.

The discrete molecular velocity distribution function f_{pi} is updated in space and time by the LBGK equation

$$f_{pi}(t + \delta t, \mathbf{x} + \mathbf{c}_{pi}\delta t) = f_{pi}(t, \mathbf{x}) + \Omega \cdot \left(f_{pi}^{\text{eq}}(t, \mathbf{x}) - f_{pi}(t, \mathbf{x}) \right). \tag{10}$$
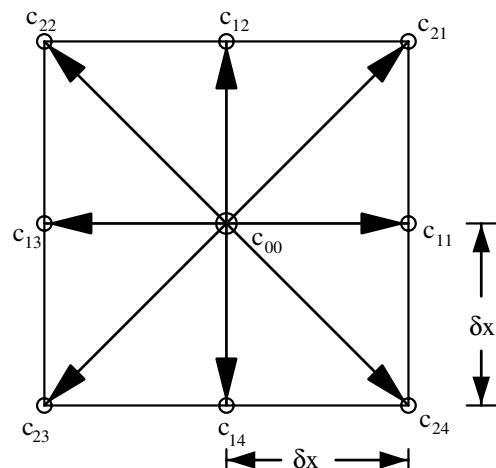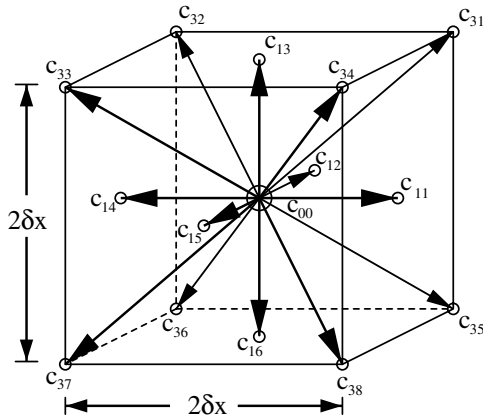

Fig. 2. 9 velocities model in 2D.

Fig. 3. 15 velocities model in 3D.

with a dimensionless collision frequency Ω. This frequency, also considered as a relaxation parameter, leads to stable calculations in the range $0 < \Omega < 2$. The frequency is associated with the kinematic viscosity of the fluid due to the relation

$$v = \left(\frac{1}{\Omega} - \frac{1}{2}\right)c_s^2 \delta t. \tag{11}$$

The equilibrium distribution function f_{pi}^{eq} is a discrete analog of the Maxwellian distribution function under the assumption of small Mach numbers. The Maxwellian, expanded for nearly incompressible flows with constant density ρ_0, [23], results in:

$$f_{pi}^{eq}(t, \mathbf{x}) = t_p \rho_0 \left[\frac{P(t, \mathbf{x})}{\rho_0 c_s^2} + \frac{u_\alpha(t, \mathbf{x})c_{pi\alpha}}{c_s^2} + \frac{u_\alpha(t, \mathbf{x})u_\beta(t, \mathbf{x})}{2c_s^2}\right.$$
$$\left. \cdot \left(\frac{c_{pi\alpha}c_{pi\beta}}{c_s^2} - \delta_{\alpha\beta}\right)\right] \tag{12}$$

The definition c_s corresponds to the isothermal speed of sound $c_s = \sqrt{RT}$ and is related to the unit lattice speed c_0 by $c_s = c_0/\sqrt{3}$. The weighting factors t_p are defined such that the invariant, macroscopic quantities are satisfied by the discrete Maxwellian and result in the symmetry properties of the discrete phase space. It is $t_p = 4/9, 1/9, 1/36$ for $p = 0, 1, 2$ in 2D and $t_p = 2/9, 1/9, 1/72$ for $p = 0, 1, 3$ in 3D. Macroscopic quantities are the hydrodynamic pressure P and the velocity components u_α with $\alpha = 1, 2, 3$ for Cartesian directions. The macroscopic variables P and u_α are be determined as the discrete zeroth and first moments of the distribution function in each node

$$P = c_s^2 \sum_{p,i} f_{pi} \quad \text{and} \quad \rho_0 u_\alpha = \sum_{p,i} f_{pi}c_{pi\alpha}$$

Analysis of this LBGK approach using Taylor series and Chapman–Enskog expansion confirms that the LBGK approach satisfies the Navier–Stokes equations of an incompressible fluid for sufficient small, discrete Knudsen numbers $\varepsilon = \delta x/L \ll 1$ and Mach numbers $M_g = U/c_0 \ll 1$, where L and U are characteristic, macroscopic lengths and velocities of the problem.

$$\frac{\partial u_\alpha}{\partial x_\alpha} = O(\varepsilon M_g)$$
$$\frac{\partial \rho_0 u_\alpha}{\partial t} + \frac{\partial \rho_0 u_\alpha u_\beta}{\partial x_\beta} + \frac{\partial P}{\partial x_\alpha} = \frac{\partial}{\partial x_\beta}\left[\mu\left(\frac{\partial u_\alpha}{\partial x_\beta} + \frac{\partial u_\beta}{\partial x_\alpha}\right)\right] + O(\varepsilon M_g) \tag{13}$$

The Stokes equations are of advantage at very low Reynolds numbers. They result from the present LBGK approach by changing the discrete Maxwellian, Eq. (12), to a linear approach

$$f_{pi}^{eq}(t, \mathbf{x}) = t_p \rho_0 \left(\frac{P(t, \mathbf{x})}{\rho_0 c_s^2} + \frac{u_\alpha(t, \mathbf{x})c_{pi\alpha}}{c_s^2}\right)$$

The resulting system of Stokes equations are

$$\frac{\partial u_\alpha}{\partial x_\alpha} = O(\varepsilon M_g)$$
$$\frac{\partial \rho_0 u_\alpha}{\partial t} + \frac{\partial P}{\partial x_\alpha} = \mu \frac{\partial^2 u_\alpha}{\partial x_\beta^2} + O(\varepsilon M_g) \tag{14}$$

The formal accuracy in space is of second order, i.e. $O(\delta x^2)$, for both the Navier–Stokes and Stokes equations, if $\varepsilon \sim M_g \ll 1$ is satisfied. The temporal accuracy is of less importance here, since the flow is stationary or only slowly changing.

3.2. LBGK method for equations of Poisson type

The present LBGK concept enables the solution of scalar potential equations of the type of Poisson or Laplace equations in a similar way as shown above for the Navier–Stokes equations. Other solution methods for Poisson equations, such as multi-grid methods, may be faster than LBGK methods, but the treatment of complex boundary conditions for electric or magnetic potentials on the filter surfaces is easier to handle by a LBGK method. In addition, the same grid, the same algorithmic structure and refinement and the same boundary value procedure can be used for flow and potential computations, as well.

Assuming, a component ϕ_α with $\alpha = 1, 2, 3$ of a vector potential $\mathbf{\Phi}$ has to be determined, which is described by a Poisson equation

$$\frac{\partial^2 \phi_\alpha}{\partial x_\beta^2} = -RS_\alpha \tag{15}$$

where RS_α is a given right hand side of a Poisson equation and ϕ_α may be the potentials of electrical or magnetic fields.

The principle of solving a Poisson equation by a LBGK method is based on that for the Stokes equations, Eq. (14), where the stress terms are in form of a Laplace operator. Therefore, only the pressure gradient has to be compensated in the steady-state form to isolate the operator. However, some modifications are still necessary to ensure stability and accuracy of the LBGK method for a Poisson equation. The potential ϕ_α is defined as the first invariant moment

$$\phi_\alpha = M_{1\alpha} = \sum_{p,i} f_{pi} c_{pi\alpha} = \sum_{p,i} f_{pi}^{eq} c_{pi\alpha}, \quad \alpha = 1, 2, 3. \qquad (16)$$

The linear equilibrium distribution is defined by

$$f_{pi}^{eq}(t, \mathbf{x}) = t_p \left[1 + \frac{\phi_\alpha c_{i\alpha}}{c_S^2} \right]$$

The definitions of the phase space (lattices) remain the same as for the Navier–Stokes equations in Figs. 2 or 3. A modified LBGK equation reads now:

$$f_{pi}(t + \delta t, \mathbf{x} + \mathbf{c}_{pi}\delta t) = f_{pi}(t, \mathbf{x}) + \Omega$$
$$\cdot \left(f_{pi}^{eq}(t, \mathbf{x}) - f_{pi}(t, \mathbf{x}) \right) + \delta t \, s_{pi} \qquad (17)$$

The source terms $\delta t \, s_{pi}$ in Eq. (17) reads

$$\delta t s_{pi} = t_p \left(1 - \frac{\Omega}{2} \right) c_{pi\alpha} \left(2 \frac{\partial M_0}{\partial x_\alpha} + \frac{\delta t}{\Omega} R S_\alpha \right)$$

The term $\frac{\partial M_0}{\partial x_\alpha}$ corrects non-equilibrium effects from the moment M_0 of the non-equilibrium distribution, which is different from its equilibrium value. The zero moment is defined as

$$M_0 = \sum_{p,i} f_{pi} \neq \sum_{p,i} f_{pi}^{eq} \qquad (18)$$

Analysis based on Taylor and Chapman–Enskog expansions, similar to that used for the Navier–Stokes equations, confirms that the equation of the first moment yields the desired Poisson equation (15) for the potential equation (16). Unlike the Poisson equation the LBGK equation is time dependent, therefore the two problems are equivalent only in the stationary state. More details of the derivation are presented in [22]. The LBGK solution results in three potentials ϕ_α in 3D, each satisfies a Poisson equation of type Eq. (15). However, the potentials are coupled with each other by the equation of the zero moment, a kind of a ''continuity equation''

$$\frac{\partial \phi_\alpha}{\partial x_\alpha} = \Omega(1 - M_0)$$

Thus the potentials ϕ_α are not independent from each other through this coupling mainly over the boundary conditions. In general only one component is usually used. Nevertheless, all algorithmic extensions of the LBGK method for fluid flow, as boundary fitting formulations from [12] or grid refinement from [13] are utilized in LBGK solutions of the Poisson equation.

The treatment of complex boundary conditions is the essential argument for solving the equations of electric or magnetic potentials by a LBGK method. Therefore validations of the LBGK-Poisson solver are performed with different types of boundary conditions for the potential around a circular cylinder. Comparisons are made with an iterative finite-difference solution for the same grid resolution. In the first case a Laplace equation is solved with Dirichlet boundary conditions at the cylinder surface and at the in- and outlet boundaries, while periodic boundary conditions are applied at the lower and upper boundaries.
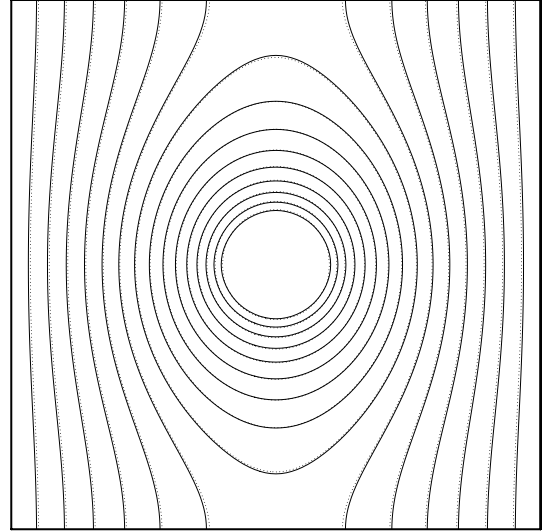

Fig. 4. Lines of constant potential from LBGK (solid lines) and finite-difference solution (dotted lines) with Dirichlet boundary conditions at the cylinder.

This problem corresponds to a two-dimensional example of the three-dimensional calculations of the electric field around a filter, shown in a later section. The lines of constant potential (solid lines) are presented in Fig. 4, compared with that of finite-difference solution (dotted lines). The same problem, but with von Neumann boundary conditions at the cylinder and Dirichlet conditions at other boundaries, is plotted in Fig. 5. Comparisons for the spatial accuracy show that the differences between LBGK and finite-difference solutions are negligible. Both, the LBGK and the finite difference solutions are of second order in space. Comparisons of computational times are not intended and thus not presented.
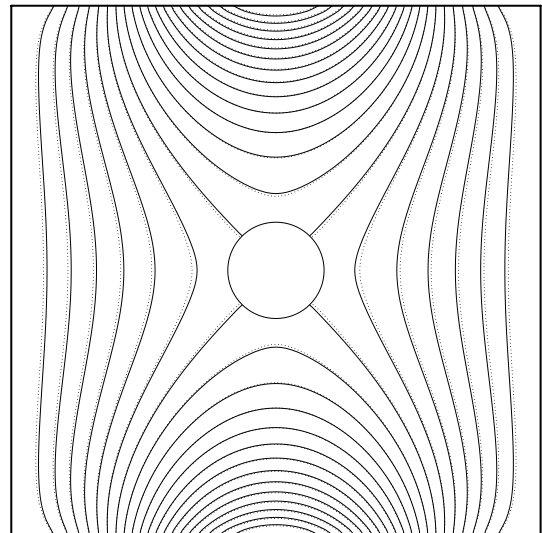

Fig. 5. Lines of constant potential from LBGK (solid lines) and finite-difference solution (dotted lines) with von Neumann boundary conditions at the cylinder.

4. Numerical validations and results

4.1. Validation of the model of random diffusion

The validity of the numerical realization of the stochastic model of the Brownian diffusion in Eq. (6) is important for the physical relevance of the complete particle Monte Carlo method. Therefore comparisons are made between the diffusion coefficients obtained from the theoretical Stokes–Einstein equation

$$D = \frac{kT}{\beta m_p} \qquad (19)$$

and with the approach in Eq. (6). The procedure is similar to that in [42].

The approach equation (6) is validated by simulating the Brownian movement of parcels (about 1000), whose initial position is the origin. They are moving only under the influence of Brownian motion with a constant time step Δt. The mean square displacement $\overline{x^2}$ is calculated from the final positions of the particles after an elapsed time period t_t. The diffusion coefficient D is determined from the computed results using the equation

$$\overline{x^2} = 6D\Delta t. \qquad (20)$$

The diffusion coefficient D is plotted against the particle diameter d_p in Fig. 6. The theoretical values according to Eq. (19) are given as full line, the computed, statistical results are plotted for different values of time periods t_t and of time steps Δt. The correspondence between the theoretical values and the computed values are found to be very well if the ratio between the time period and the time step is large enough. In the case of the square symbols the time period for diffusion is too small. After the time period is

Fig. 6. Comparison between the calculated diffusion coefficient D and its theoretical value from the Stokes–Einstein equation.

increased by a factor of 30 the discrepancy is disappeared (circular symbols).

4.2. Particle motion through fibrous filters

The gas–particle flow through fibrous filters and the particle deposition for particles of diameters larger than 0.5 μm was considered by the authors in former publications [11,14,31]. The motion of such "large" particles is influenced essentially by inertia forces, the corresponding particle trajectories are deterministic.

In contrast to that, the present consideration deals with small particles in the diameter range of nanometers, i.e. of diameters smaller than 100 nm. The effect of inertia forces becomes smaller in this range, but random diffusion and thus the Brownian random motion of particles plays an increasing role.

Fiber filters are considered here as test geometries. The geometrical arrangement of a three-dimensional model filter consists of a layer of fibrous filter, as shown in Fig. 9. The filter layer is formed by crossing wires of circular cross-section. The numerical domain of integration is a rectangular box around the layer of fibers assuming periodic boundary conditions in y and z directions which simulates an infinite extension of the filter mat to the sides and above and below. In general, the grid consists of 761,807 nodes. The diameter of the fiber in lattice units is $d_f^* = d_f/\delta x = 6.5$. Local grid refinement with factor six is employed in the vicinity of the filter surface to achieve a higher resolution near the surfaces, where particles are depositing. The inflow direction is the x-direction with flow from the left to the right, see Fig. 9. The particles start at a position $\mathbf{x}_0 = (x_0, y_0, z_0)$ where y_0 and z_0 are chosen randomly using an equal distribution in the y, z-plane and x_0 is chosen as 142.5 μm, i.e. about twice the fiber diameter, in front of the filter surface. It guarantees that the fluid velocity and thus the particle concentration is nearly undisturbed due to the filter. The initial particle speed is equal the streaming velocity at its initial position.

The fluid field is calculated by the lattice-Boltzmann method for a Reynolds number of $Re = 0.89$, determined from the mean fluid velocity $u_\infty = 0.2126$ m/s and the diameter of the fiber $d_f = 65$ μm. The interaction between the deposited particles and the fluid field or the electric field respectively is taken into account iteratively.

The calculation of the particle motion is performed by the integration of the Langevin equation (3), as described in the previous section. The stochastic motion of the Brownian motion is realized by corresponding random numbers, as defined in Eq. (6). The time step for integrating the particle equation (4) is between 3×10^{-11} and 1×10^{-10} s and the time period of the simulation is in the range of 4.5×10^{-7} and 3.5×10^{-6} s. The calculated particle transport takes into account gas velocity and the electric field, if required. In the neighborhood of the surfaces, the deposition of the particles is influenced by van der Waals forces or image forces in the case of charged particles.
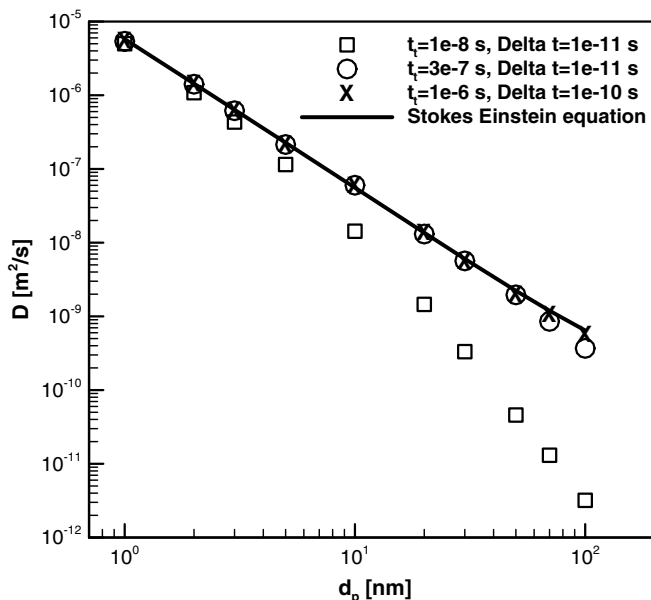
Multiple solutions with different initial configurations and moderate numbers of particles are computed instead of one field with very large numbers of particles. This procedure saves computer memory but requires averaging of the single solutions to achieve reliable statistical results for integrated values as e.g. the penetration value.

4.2.1. Validation of particle filtration with experimental data

Comparison is made with experimental data for particle deposition in fibrous filters [30]. The experiments are performed with particles between 9 and 20 nm diameter and a fiber diameter of the filter of 65 μm. Nitrogen at one atmosphere and 298 K is used as the carrying phase and the volume flow varies between 0.5 and 2.0 l/min. The penetration is defined as ratio between the amount of particles flying through the filter, i.e. of non-deposited particles, and the total amount of particles. This value is measured after a pre-defined time of the gas–particle flow. Numerically, the values of penetration are obtained by averaging the results of five simulations for one fiber grid, each with 10,000 particles. To calculate the value of penetration for the whole filter, as measured in experiments, the value of one grid has to be exponentiated with the number of filter grids used in the experiment. It results from the assumption that the distance between two filter grids is large enough to ensure identical inflow velocities for each grid. Fig. 7 shows the values of penetration for 20 grid levels as a function of the particle diameter and the volume flow. The computed results take into account the Brownian random diffusion, the van der Waals forces and the drag forces. The simulated results, shown in Fig. 7 as lines, agree well with the experimental data (symbols), plotted for different volume fluxes. The penetration is low for small particles and grows with increasing particle size. Reduction of the volume flow

and therefore the mean streaming velocity leads to decreasing penetration. Because the ratio between the diameters of the fiber and the particles is large the influence of earlier deposited particles on the deposition process can be neglected.

4.2.2. Limiting ranges of filter collection efficiency

The collection efficiency is defined as the ratio between deposited particles and the total amount of particles and is therefore directly related to the penetration as one minus penetration.

The demonstrative case in Fig. 8 illustrates the dependence between the filter collection efficiency and the particle diameter over a range which includes the physical limits of particle filtration, the diffusion and the interception limit. The particle transport and deposition is determined here by the fluid flow, by the Brownian motion and by van der Waals forces near surfaces. The particle diameter is varied here from 1 to 30 nm. The diameter of the fiber is decreased to 650 nm in comparison to previous examples to save computational time and to increase the probability of deposition on earlier deposited particles. To obtain the Reynolds number $Re = 0.89$ and Peclet number $Pe = u_\infty d_f/D$ with the streaming velocity u_∞ the fiber diameter d_f and the diffusion coefficient D the fluid speed is set to 21.26 m/s. The calculated values are obtained from 60,000 particles moving in the fluid. For decreasing diameter the collection efficiency decreases slowly up to a minimum value at 8 nm. The reason for this effect is the direct interception which influences the particle deposition due to the growing particle radius. For particle diameters smaller than 8 nm the collection efficiency grows rapidly due to the increasing influence of the Brownian motion. The two straight lines show the asymptotic limits for diffusion (solid line, $\propto D^{2/3}$) and direct interception (dashed line, $\propto r_p^2$),
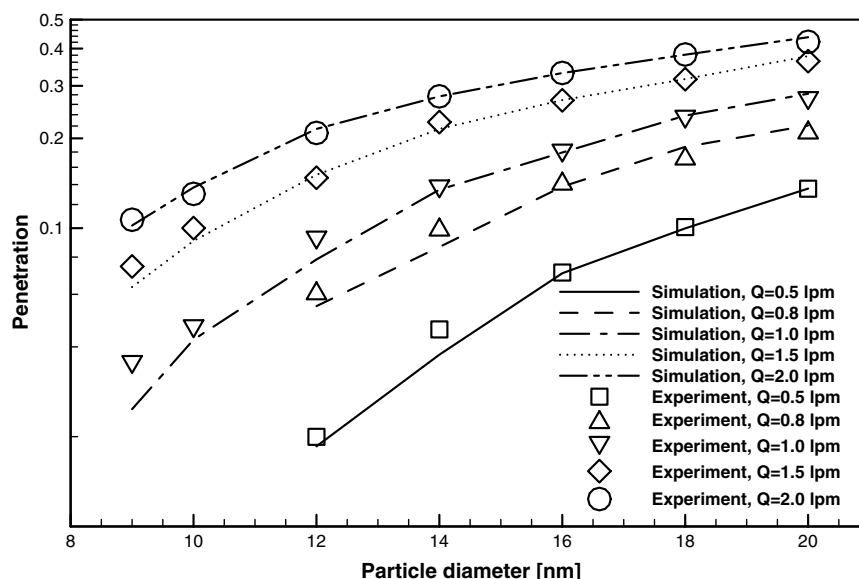

Fig. 7. Comparison between calculated penetration influenced by different volume flows and experimental values.
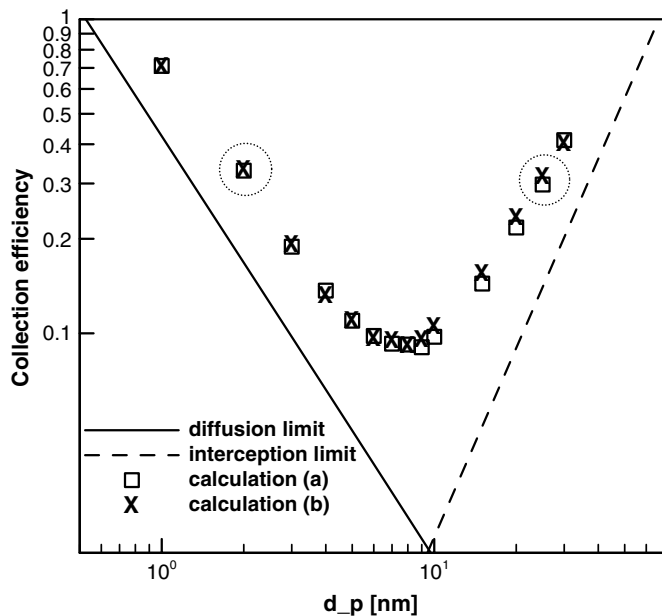
Fig. 8. Calculated collection efficiency for different particle diameters with a fiber diameter of 650 nm at $Re = 0.89$. Comparison of calculated values with (a) and without (b) changing boundaries and asymptotic limits. Circles correspond to depositions shown in Figs. 9 and 10.

which are valid for small Stokes numbers $Stk = \frac{2u_\infty}{d_f \beta}$, see [16]. The computations cover the range of Stokes numbers from 0.0001 to 0.09. Since the asymptotes left and right are estimated for single fibers, they do not take into account the real filter geometry, i.e. the interfiber distance. The

asymptotes are therefore adjusted to the particular case by multiplication with a constant value. The gradients of the calculated curve agree well with these limits. The repeated consideration of deposited particles as changed boundary contour for the fluid field in calculation (a) has nearly no influence on the deposition process. Only for particles larger than 8 nm there is a slightly difference in the collection efficiency, i.e. it is larger in the case of the fixed fluid field (calculation (b)).

Figs. 9 and 10 show two examples of deposited particle structures on filter surfaces for two limiting cases marked in Fig. 8 by circles. The structures are obtained from simulations of the particle transport under influence of flow convection, of Brownian motion and of van der Waals forces. Changed boundary conditions of the fluid flow due to deposited particles are taken into account by recalculating the fluid field with new boundary conditions each time, when 50 particles are deposited. The simulations are performed for particle diameters of 2 nm in Fig. 9 and of 25 nm in Fig. 10 with corresponding diffusion coefficients of $D_2 = 1.514 \times 10^{-6}$ m^2/s and $D_{25} = 6.249 \times 10^{-9}$ m^2/s.

Initially, 60,000 particles are started in both cases leading to nearly the same value of collection efficiency. Fig. 9 shows the case of smaller particles (left circle in Fig. 8) with 18,783 deposited particles of diameter of 2 nm. The corresponding result for 25 nm diameters (right circle in Fig. 8) is illustrated in Fig. 10 with 17,862 deposited particles. In both cases irregular dendrite like formations arise. Since for smaller particles the displacement due to Brownian motion is larger, the structures shown
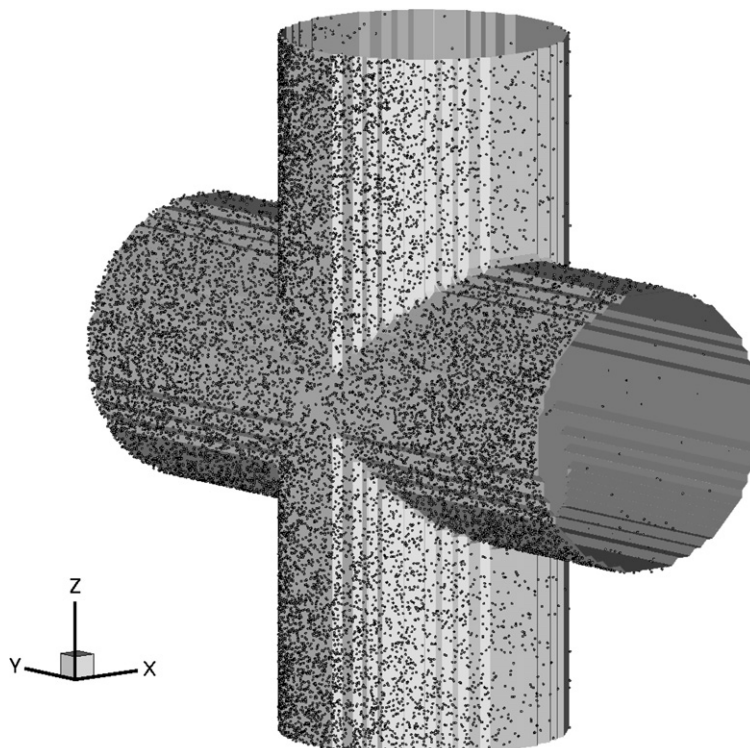

Fig. 9. Deposited layer consisting of 18,783 deposited particles with a diameter of 2 nm, penetration is 0.687.
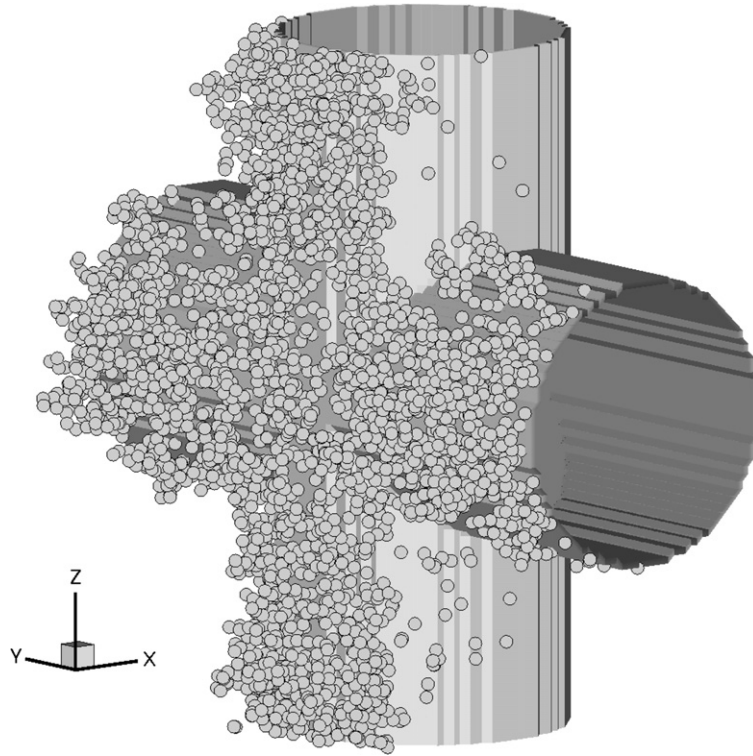
Fig. 10. Deposited layer consisting of 17,862 deposited particles with a diameter of 25 nm, penetration is 0.7023.

in Fig. 9 are less dense than the ones formed by the larger particles. The penetration for 2 nm particles is 0.687 whereas it is 0.702 for 25 nm particles. The ratio between the mean particle displacement due to fluid speed and due to diffusion force (Brownian motion) is 0.05 for the smaller particles, whereas it is 0.57 for the larger ones.

4.2.3. Influence of additional electric force

Electrically charged particles enable a better control of deposition and higher filter efficiency, as well. The influence of electric forces on charged particles is taken into account together with fluid convection, Brownian motion and van der Waals forces. The electrical Coulomb force $\mathbf{F}_{cou}$ is given by Eq. (7) where the electric potential ϕ is the solution of a Laplace equation

$$\Delta\phi = 0.$$

The solution of the Laplace equation is performed with the modified LBGK model, described in Section 3.2. The advantage of using the LBGK method, compared to usual Poisson solvers, is the flexible way to deal with complex boundary geometries.

The electrical potential is prescribed by Dirichlet boundary conditions with a value of ϕ_0 at surfaces, generally oppositely charged as particles. Oncoming particles take immediately the potential of the surface, when they deposit. Similar to the displacement of flow by deposited particles, the deposited particles change here the geometry of the boundary, where the potential is $\phi = \phi_0$. To take into account this influence, the calculation of the electric

potential is repeated with the new boundary after each 50th deposited particle, similar to the procedure for the flow field. One example of potential calculation is given in the following figures. Fig. 11 shows the equipotential surfaces of the electric potential around a filter grid.

The influence of the electric field on charged particles is demonstrated in the next figures. For reasons of enhancement of the Brownian motion the diameter of the particle is chosen to 10 nm and of the fiber to 65 μm with a fluid speed of 0.2126 m/s. Fig. 12 shows first the trajectory of a non-charged particle after 180,000 time steps under the influence of the fluid field, van der Waals forces and Brownian diffusion. The latter one can be observed as irregular random motion. The same calculation is repeated, but now additionally under the influence of attracting electric force of an electric field strength of 600 kV/m, Fig. 13. The initial position of the particle is identical for both cases whereas the particle is deposited on the filter in the case of the attracting electric force and it is going through else. Under the influence of this electric field the diffusive motion of the charged particle is much reduced. The calculation takes only 37032 time steps. After calculation of the trajectories of 60000 particles influenced by an attracting electrical force with $d_p = 10$ nm $d_f = 650$ nm and $u_\infty = 21.26$ m/s the penetration is 0.6793 with recalculation of the fields and 0.6821 without it. Neglecting the electric forces results in a penetration factor of 0.9025. Fig. 14 shows the deposited layer after 19,244 deposited particles and after recalculation of fluid field and electric field. It is obvious that the dendrite-like formations of the deposited particles are
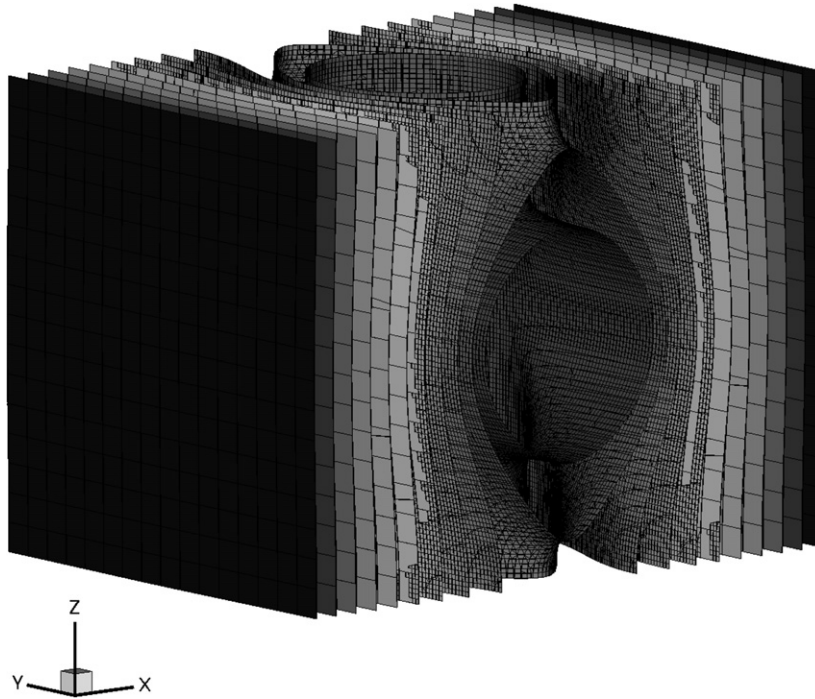
Fig. 11. Equipotential surfaces of the electric potential.
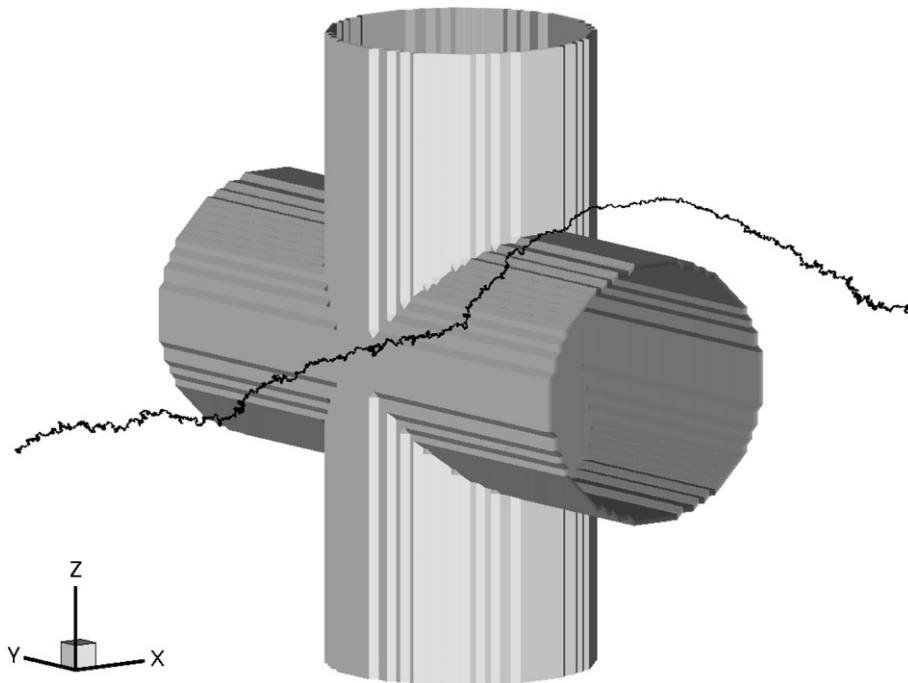

Fig. 12. Trajectory of a 10 nm particle under influence of the fluid flow, Brownian motion and van der Waals forces.

larger than in the case of no electric forces (Fig. 9). The influence of the deposited particles on the electric potential is illustrated in Fig. 15. The electric potential shows an obvious disturbance versus Fig. 11 due to the changed surface. To emphasize the influence of the changed boundary conditions on the deposition process of the particles a demonstrative, perhaps not so realistic simulation is per-

formed and shown in Fig.16. In the first case (lower part) the Coulomb force acting on the particle is calculated by the electric potential of the clean filter surface. The particle is attracted and deposits at the rear. If the earlier deposited particles keep their own (negative) potential the electric force around the fiber is strongly changed (upper part). This force acts rejecting at the front and attracting at the
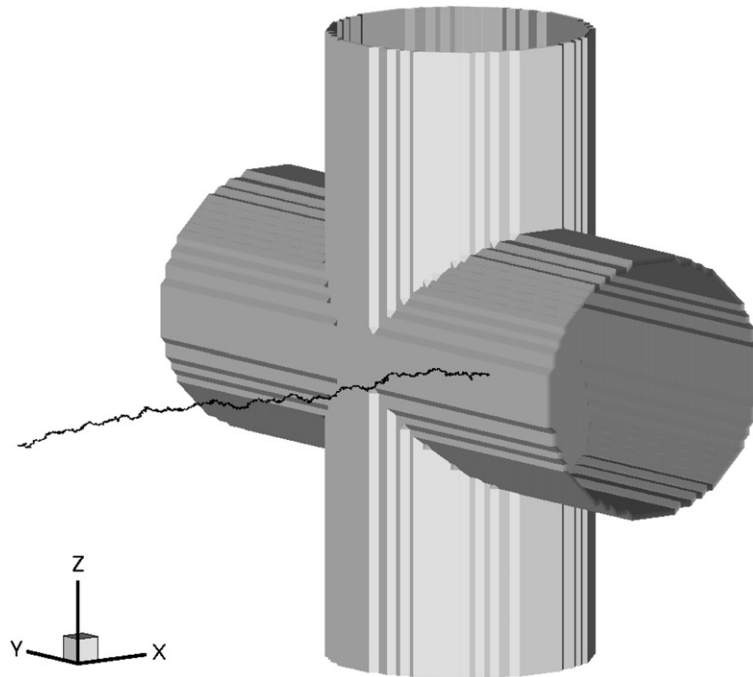
Fig. 13. Trajectory of a 10 nm particle under additional influence of an electric field.
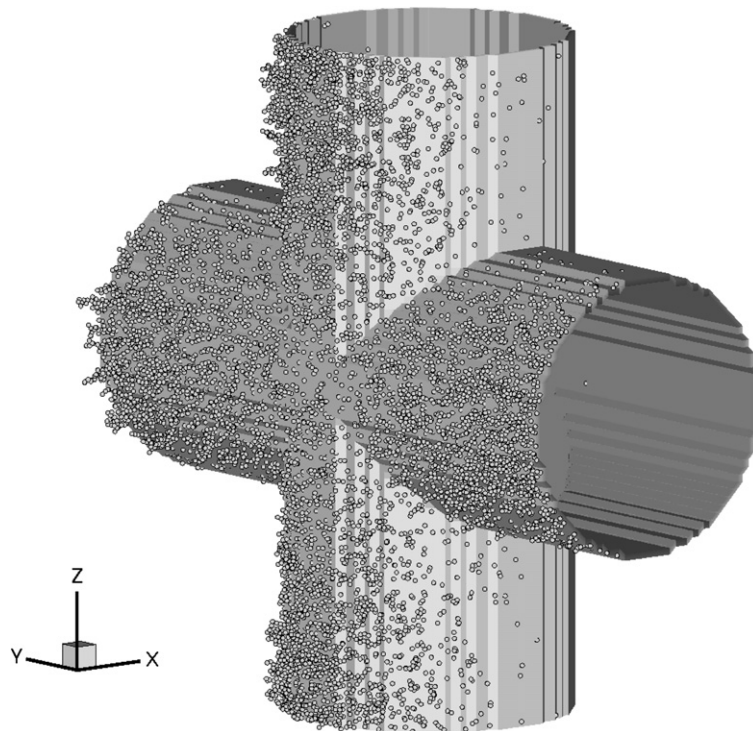

Fig. 14. Deposited layer consisting of 19,244 deposited particles with a diameter of 10 nm under consideration of an attracting electric force, penetration is 0.6793.

rear part. The effect is illustrated by the (light) trajectory in Fig. 16, the particle does not deposit at the filter surface. The test particle starts at the same position in both cases. The case with the undisturbed electric potential is mirrored by the dashed line for better visualization. This example shows that the deposited particles can modify the electric field due to the changes of the geometry or due to the changes of the potential at the surfaces.
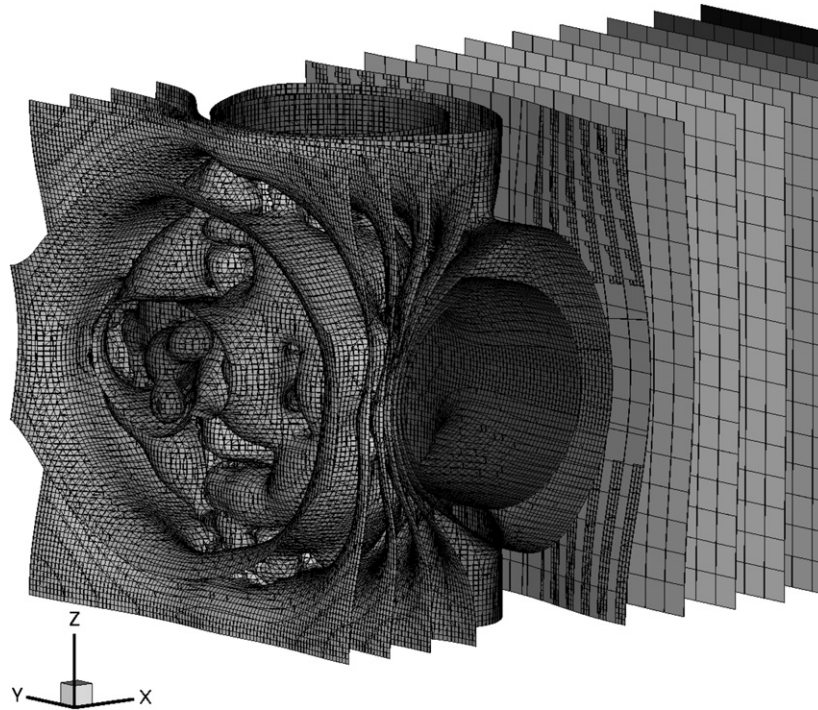
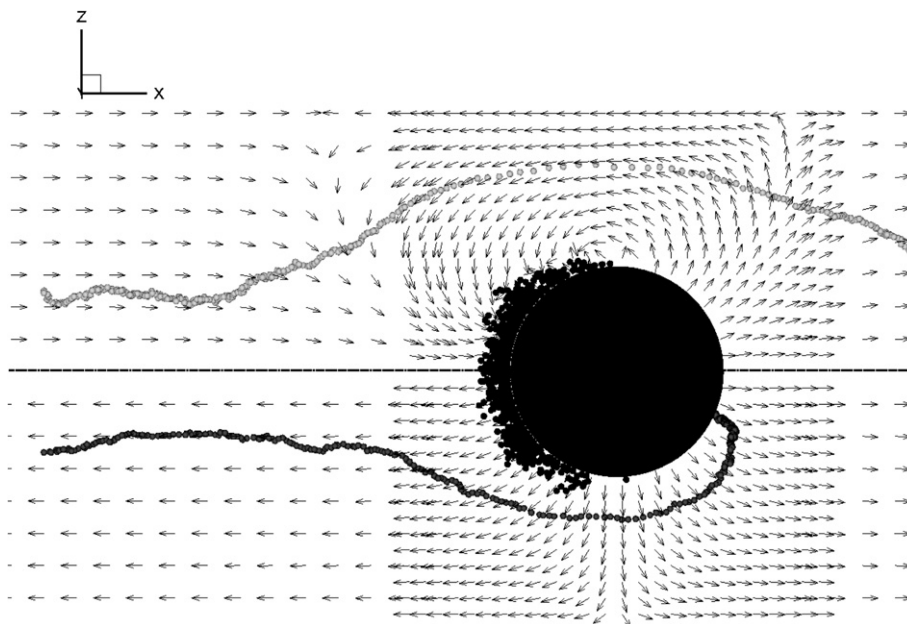Fig. 15. Disturbed equipotential surfaces of the electric potential due to deposited particles.

Fig. 16. Particle trajectories and vectors of the electric field with (light) and without (dark) influence of the deposited particles.

4.3. Deposition of charged particles on a flat plate

The strong influence of electric forces is demonstrated by an simulation of deposition of charged particles on a flat plate with different electric potentials. The main part of the plate is for example positive charged, while the narrow stripe in the middle has the other potential. The electrical potential is determined from Eq. (15) on a Cartesian grid of 127,970 nodes. The boundary conditions at the lateral boundaries are extrapolated and the same potential as on the main part of the plate is assumed on the upper boundary.

Oncoming particles are either positively or negatively charged. The particles start at the top of the integration domain and move due to the different forces towards the plate. Their movement is influenced by Brownian motion,
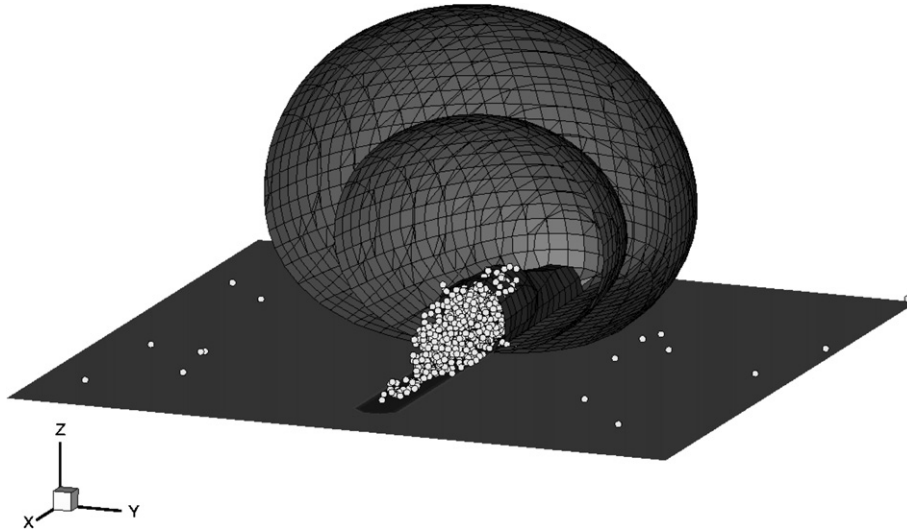
Fig. 17. Iso-surfaces of the electric potential and deposited layer after 1000 deposited 80 nm particles influenced by an attracting electric force.
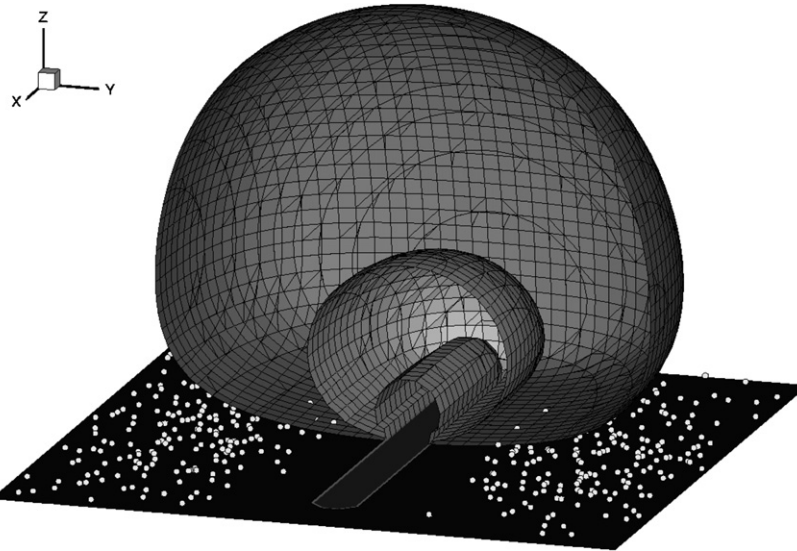

Fig. 18. Iso-surfaces of the electric potential and deposited layer after 1000 deposited 80 nm particles influenced by a repulsive electric force.

by Coulomb forces and by drag forces. Image forces and van der Waals forces are acting additionally in the vicinity of the surface.

Fig. 17 shows the deposition behavior for opposite charged middle stripe and particles. The particles are attracted essentially by the stripe and deposited there. The electric potential of the deposited particle is taken from the place where it touches the surface, i.e. the plate or an earlier deposited particle. Therefore it changes the boundary conditions for the potential as seen by the iso-surfaces of the electric potential. Fig. 18 illustrates the deposited layer for the same parameters but with rejecting electric forces in the middle range. Most of the particles are deposited outside of the stripe.

5. Conclusion

The paper presents a numerical solution concept for simulating the transport and deposition process of small particles in complex geometries. Complex geometries mean here any given filter geometries but also disturbed surface geometries by deposited particles, which form very irregular surface structures. The relatively easy consideration of such irregular boundaries is one advantage of the lattice-Boltzmann (LBGK) methods. These methods are presented here for solutions of fluid flow (Navier–Stokes and Stokes equations) and as a new development for solutions of electrically or magnetic potential fields (Poisson-type equations). Flow and potential solution are used to define

drag and electrical forces acting on particles. The trajectories of single particles are calculated with a so-called particle Monte Carlo method, taking into account additional forces as random forces due to Brownian movement and van der Waals forces, acting essentially in the vicinity of rigid surfaces. The solution concept is demonstrated by number of examples. It has been shown that changing boundary conditions of the fluid field have nearly no influence on the deposition process for particles with a diameter of $O(10 \text{ nm})$ whereas the recalculation of the electric field has an essential effect on the deposition rate of the particles. The present concept offers an efficient way to deal with the complex particle processes. Extensions of the method are in progress and under validation, taking into account particle rotation under fluid, magnetic and random torques.

Acknowledgement

References

[1] Abe T. Derivation of the lattice Boltzmann method by means of the discrete ordinate method for the Boltzmann equation. J Comput Phys 1997;131:241–6.

[2] Bhatnagar P, Gross EP, Krook MK. A model for collision processes in gases. I. Small amplitude processes in charged and neutral one-component systems. Phys Rev 1954;94:511–25.

[3] Brown RC. Air filtration, an integrated approach to the theory and applications of fibrous filters. Pergamon Press; 1993.

[4] Chandrasekhar S. Stochastic problems in physics and astronomy. Rev Mod Phys 1943;15:1–89.

[5] Chang YI, Whang JJ. Particle deposition behavior simulated by the stochastic method. J Pet Sci Engr 1999;22:189–203.

[6] Chen H, Chen D, Matthaeus W. Recovery of the Navier–Stokes equations through a lattice gas Boltzmann equation method. Phys Rev A 1992;45:R5339–42.

[7] Chen S, Cheung CS, Chan CK, Zhu C. Numerical simulation of aerosol collection in filters with staggered parallel rectangular fibres. Comput Mech 2002;28:152–61.

[8] Dupuis A, Chopard B. Lattice gas modeling of scour formation under submarine pipeline. J Comput Fluids 2002;16:523–32.

[9] Elimelech M, Gregory J, Jia X, Williams R. Particle deposition and aggregation—measurement, modelling and simulation. Oxford: Butterworth-Heinemann Ltd.; 1995.

[10] Ermak DL, Buckholz H. Numerical integration of the Langevin equation: Monte Carlo simulation. J Comput Phys 1980;35:169–82.

[11] Filippova O, Hänel D. Lattice-Boltzmann simulations of gas–particle flow in filters. Comput Fluids 1997;7:697–712.

[12] Filippova O, Hänel D. Boundary fitting and local grid refinement for lattice-BGK models. Int J Mod Phys C 1998;9:1271–9.

[13] Filippova O, Hänel D. Grid refinement for lattice-BGK models. J Comput Phys 1998;147:219–28.

[14] Filippova O, Hänel D. Numerical simulation of gas–particle flow in filters by lattice Bhatnagar–Gross–Krook model. In: Spurny KR, editor. Advances in aerosol filtration. Boston, London, New York: Lewis Publishers; 1998.

[15] Filippova O, Hänel D. Acceleration of lattice-BGK schemes with grid refinement. J Comput Phys 2000;165:407–27.

[16] Friedlander SK. Smoke, dust, and haze—fundamentals of aerosol dynamics. Oxford University Press; 2000.

[17] Gschaider BFW, Honeger CC, Redl CEP. Soot particle deposition within porous structures using a method of moments—lattice Boltzmann approach. In: Bubak M et al., editors. ICCS-04, Kracow, June 6–9, 2004. Berlin: Springer-Verlag; 2004.

[18] Ginzburg I, d'Humieres D. Local second order boundary methods for lattice Boltzmann models. J Stat Phys 1996;84:927–71.

[19] Ginzburg I, d'Humieres D. Multireflection boundary conditions for lattice Boltzmann models. Phys Rev E 2003;68:066614.

[20] Gupta D, Peters MH. A Brownian dynamics simulation of aerosol deposition onto spherical collectors. J Colloid Interface Sci 1985;104:375–89.

[21] Hänel D. Molekulare gasdynamik. Berlin, Heidelberg, New York: Springer-Verlag; 2004.

[22] Hänel D, Lantermann U, Kaiser R, Wlokas I. Generalized lattice-BGK concept for thermal and chemically reacting flows at low Mach numbers. Int J Numer Meth Fluids, in press.

[23] He X, Luo LS. Lattice Boltzmann model for the incompressible Navier–Stokes equation. J Stat Phys 1996;88:927–44.

[24] He X, Luo LS. A priori derivation of the lattice Boltzmann equation. Phys Rev E 1997;55:R333–6.

[25] Higuera F, Succi S, Benzi R. Lattice gas dynamics with enhanced collisions. Europhys Lett 1989;9:345–9.

[26] d'Humieres D. Generalized lattice Boltzmann equations. In: Shizgal D et al., editors. RGD, Prog Astronaut Aeronaut, vol. 159; 1992. p. 450–8.

[27] d'Humieres D, Ginzburg I, Krafczyk M, Lallemand P, Luo LS. Multiple-relaxation-time lattice Boltzmann models in three dimensions. Philos Trans R Soc London A 2002;360:437–51.

[28] Israelachvili J. Intermolecular & surface forces. Academic Press; 1997.

[29] Karatzas I, Shreve SE. Brownian motion and stochastic calculus. Springer-Verlag; 1988.

[30] Kauffeldt T. Personal communication, 2004.

[31] Krafczyk M, Lehmann P, Filippova O, Hänel D, Lantermann U. Lattice Boltzmann simulations of complex multiphase flows. In: Sändig AM et al., editors. Multifield problems—state of the art. Springer-Verlag; 2000.

[32] Lallemand P, Luo LS. Theory of the lattice Boltzmann method: dispersion, dissipation, isotropy, Galilean invariance, and stability. Phys Rev E 2000;61:6546–62.

[33] Masselot A, Chopard B. A lattice Boltzmann model for particle transport and deposition. Europhys Lett 1998;42:259–64.

[34] McNamara G, Zanetti G. Use of the Boltzmann equation to simulate lattice-gas automata. Phys Rev Lett 1988;61:2332–5.

[35] Mei R, Luo LS, Shyy W. An accurate curved boundary treatment in the lattice Boltzmann method. J Comput Phys 1999;155:307–30.

[36] Oh YW, Jeon KJ, Jung AI, Jung YW. A simulation study on the collection of submicron particles in a unipolar charged fiber. Aerosol Sci Technol 2002;36:573–82.

[37] Przekop R, Moskal A, Gradoń L. Lattice-Boltzmann approach for description of the structure of deposited particulate matter in fibrous filters. J Aerosol Sci 2003;34:133–47.

[38] Qian YH, d'Humiéres D, Lallemand P. Lattice BGK models for Navier–Stokes equation. Europhys Lett 1992;17:479–84.

[39] Tien C. Granular filtration of aerosols and hydrosols. Butterworth Publishers; 1989.

[40] Wu Z, Walters JK, Thomas DWP. The deposition of particles from an air flow on a single cylindrical fiber in a uniform electric field. Aerosol Sci Technol 1999;30:62–70.

[41] Yu D, Mei R, Luo LS, Shyy W. Viscous flow computations with the method of lattice Boltzmann equation. Progr Aerospace Sci 2003;39:329–67.

[42] Zarutskaya T, Shapiro M. Capture of nanoparticles by magnetic filters. J Aerosol Sci 2000;31:907–21.